Astronomy & Astrophysics manuscript no. SMC February 2, 2008
(DOI: will be inserted by hand later)

Synoptic study of the SMC SNRs using *XMM-Newton*

K.J. van der Heyden[1], J.A.M. Bleeker[1], J.S. Kaastra[1]

SRON National Institute for Space Research, Sorbonnelaan 2, 3584 CA Utrecht, The Netherlands
email: K.J.van.der.Heyden@sron.nl

Received ; accepted

Abstract.
We present a detailed X-ray spectral analysis of 13 supernova remnants (SNR) in the Small Magellanic Cloud (SMC). We apply both single-temperature non-equilibrium ionisation models and models based on the Sedov similarity solution, where applicable. We also present detailed X-ray images of individual SNRs, which reveal a range of different morphological features. Eight remnants, viz DEM S 32, IKT 2, HFPK 419, IKT 6, IKT 16, IKT 18 and IKT 23, are consistent with being in their Sedov evolutionary phase. IKT 6 and IKT 23 both have a clear shell like morphology with oxygen-rich X-ray emitting material in the centre. We draw attention to similarities between these two remnants and the well studied, oxygen-rich remnant IKT 22 (SNR 0102-72.3) and propose that they are more evolved versions of IKT 22. IKT 4, IKT 5, DEM S 128 and IKT 5 are evolved remnants which are in, or in the process of entering, the radiative cooling stage. We argue that the X-ray emission from these four remnants is most likely from the ejecta remains of type Ia SNe. Our modeling allow us to derive estimates for physical parameters, such as densities, ages, masses and initial explosion energies. Our results indicate that the average SMC hydrogen density is a factor of ~ 6 lower as compared to the Large Magellanic Cloud. This has obvious implications for the evolution and luminosities of the SMC SNRs. We also estimate the average SMC gas phase abundances for the elements O, Ne, Mg, Si and Fe.

Key words. ISM: shock waves, nucleosynthesis, abundances, supernova remnants – ISM: –X-rays

1. Introduction

The low interstellar absorption and relative closeness of the Large and Small Magelanic Clouds (LMC and SMC) allows for the study of individual X-ray sources in these galaxies. For supernova remnants (SNRs) in particular, the low absorption makes it possible to detect X-rays in the important 0.5–3.0 keV energy band, which includes emission lines from highly ionised elements such as O, Ne, Mg, Si, S and Fe. The well known distance of the SMC allows for good estimates of quantities such as physical size, mass, age and so on.

While the LMC SNRs have been relatively well studied, the remnants in the SMC have not received much attention. For example, Hughes et al. (1998) conducted a systematic study of ASCA-SIS spectra of 7 SNRs in the LMC, while Nishiuchi (2001) analysed 9 fainter remnants. They were able to derive good estimates for the physical parameters of individual SNRs. In contrast, detailed X-ray studies of the SMC have been limited to the youngest and brightest SNR, IKT 22 (SNR 1E 0102-72.3). This is mainly because SNRs in the SMC are fainter than their LMC counterparts.

To date a total of 16 SNRs have been identified from a number of extensive X-ray surveys with the instruments aboard the *Einstein*, *ASCA* and *ROSAT* Observatories (e.g. Inoue et al. 1983; Wang & Wu 1992; Haberl et al. 2000). The availability of the *Chandra* and *XMM-Newton* Observatories now provides an opportunity to study these remnants with far greater sensitivity and spatial/spectral resolution than before.

We present *XMM-Newton* observations of 13 SNRs in the SMC. The major emphasis of this work is on the spectral analysis of the CCD-resolution data obtained with the European Photon Imaging Cameras (EPIC) (Turner et al. 2001; Strüder et al. 2001). In addition, we also present high resolution spectra of IKT 22 and IKT 23 as measured by the Reflection Grating Spectrometers (RGS) (den Herder et al. 2001).

2. Observations and Reduction

Our data are extracted from five pointings towards the SMC. The log of the observations are given in Table 1. The pointings, as listed in Table 1, are centred on the remnants IKT 5, IKT 18, IKT 23 and IKT 22 respectively.

The raw EPIC data were initially processed with the *XMM-Newton* Science Analysis System (SAS) version 5.4. This involved the subtraction of hot, dead, or flickering pixels, and the removal of events due to electronic noise. The spectra were extracted using the SAS task EVSELECT. We used the standard

Send offprint requests to: K.J. van der Heyden

Table 1. *XMM-Newton* EPIC observation log.

Rev Nr	Obs ID	Mode		Filt.	Exp. (ks)	
		pn	MOS		pn	MOS
156	0110000101	EF	FF	M	23	27
157	0110000201	EF	FF	M	16	20
157	0110000301	EF	FF	M	31	35
247	0135720601	FF	LW	T	16	33
433	0135720901	FF	LW	T	14	13

Abbreviations used

EF	Extended Full Frame
FF	Full Frame
LW	Large Window
T	Thin filter
M	Medium Filter

Table 2. Log of the SNRs in our field.

Object *	SNR Cat.	Obs. ID	RA (J2000)	DEC (J2000)
DEM S 32	0044-73.4	0110000101	00 46 39.1	-73 08 39
IKT 2	0045-73.4	0110000101	00 47 12.2	-73 08 26
HFPK 419		0110000101	00 47 40.6	-73 09 30
IKT 4	0046-73.5	0110000101	00 48 24.8	-73 19 24
IKT 5	0047-73.5	0110000101	00 49 06.9	-73 14 05
IKT 6	0049-73.6	0110000101	00 51 06.5	-73 21 26
IKT 16	0056-72.5	0110000201	00 58 16.4	-72 18 05
IKT 18	0057-72.2	0110000201	00 59 25.4	-72 10 10
IKT 21	0101-72.4	0123110201	01 03 12.8	-72 08 59
IKT 22	0102-72.3	0123110201	01 04 02.0	-72 01 48
IKT 23	0103-72.6	0110000301	01 05 03.5	-72 22 56
DEM S 128		0123110201	01 05 23.2	-72 09 26
IKT 25	0104-72.3	0123110201	01 06 14.3	-72 05 18

* Abbreviations used

DEM S	Hα catalogue of emission nebulae (Davies et al. 1976)
IKT	X-ray catalogue (Inoue et al. 1983)
HFPK	X-ray catalogue (Haberl et al. 2000)

redistribution matrices available on the VILSPA site, while the ancillary matrices were created using the SAS task ARFGEN. Background subtraction was done by selecting blank sky regions within the same observation.

Mosaic images of the SMC fields were created using our own image and mosaicing software. The image extraction programme selects the photons with the appropriate grades and quality flags and saves the images in FITS file format. The latter is necessary in order to use the standard SAS EEXMAP programme to make exposure maps for each extracted image. EEXMAP produces exposure maps normalized to the on axis exposure time, so each exposure map was multiplied with the appropriate EPIC-pn or EPIC-MOS effective area by the mosaicing programme. The routines were called from a script that applied those programmes to each event-list and each channel range.

We also have high resolution spectra of IKT 22 and IKT 23 in addition to the CCD-resolution spectra. RGS spectra of IKT 22 and IKT 23 were obtained with effective exposure times of 70 and 37 ks respectively. The RGS data were processed with SAS version 5.4.

3. Analysis and Results

3.1. Images

In Fig. 1 we present a mosaic of our observations. The left image is a mosaic of *XMM-Newton* revolutions 157, 247 and 433, while the right image shows the southwestern part of the SMC (Rev 156). We are able to identify 13 SNRs in our field, these are indicated in Fig. 1 and listed in Table 2. All the remnants are quite soft X-ray sources, with the peak of their emission in the 0.5–1.0 keV band. A number of point sources, which generally display much harder spectra than the remnants, are also visible in the field-of-view. We present detailed colour coded maps of each remnant in Fig. 2. It is clear from Fig. 2 that the remnants exhibit a range of different morphological features. The physical intepretation of these morphologies will be discussed in more detail in Sect. 4.1.

3.2. Spectral Analysis

The spectral analysis was performed using the SRON SPEX package (Kaastra et al. 1996), which contains the MEKAL atomic database (Mewe et al. 1995) for thermal emission. Also contained in SPEX are a number of plasma models appropriate for SNR analysis.

We extracted spectra from the entire region of each SNR, while the background spectra were taken from nearby blank-sky regions. The spectra of individual remnants are shown in Figs. 3 and 4. A typical background spectrum is also displayed in Fig. 4. All our SNR spectra are thermal in nature and show emission from highly ionised atoms of O, Ne, Mg, Si and Fe.

We first attempted to fit all the spectra with a single temperature non-equilibrium ionisation (NEI) model. This assumes that the plasma has been instantly shock-heated to a temperature $T_{\rm e}$ some time (t) ago. The NEI model does not contain any dynamical model for SNR evolution. In this model we fit the volume emission measure ($n_{\rm es}n_{\rm Hs}V$), the electron temperature ($kT_{\rm e}$), the ionisation parameter ($n_{\rm es}t$), the elemental abundances and the column density $N_{\rm H}$ of absorbing gas along the line of sight. $n_{\rm es}$ and $n_{\rm Hs}$ are the electron and hydrogen density of the shocked gas, respectively and V is the volume of emitting gas. A distance of 60 kpc to the SMC is assumed. IKT 21 has a pulsar (AX J0103-722) in the field. We have added a power-law component to account for the pulsar emission.

During the fitting procedure we initially kept the abundances fixed at the mean SMC ISM value of 0.2 solar (Russel and Dopita 1992). We started by allowing only the normalisations of the plasma components to vary and subsequently we also allowed the temperature, ionisation age, absorption and abundances (where necessary) to vary. The spectra from EPIC-pn and EPIC-MOS were fitted simultaneously. The results of the fits are given in Table 3. The abundances are all relative to their solar values (Anders & Grevese 1989). We give the unabsorbed luminosities in the 0.5–2.0 keV band.

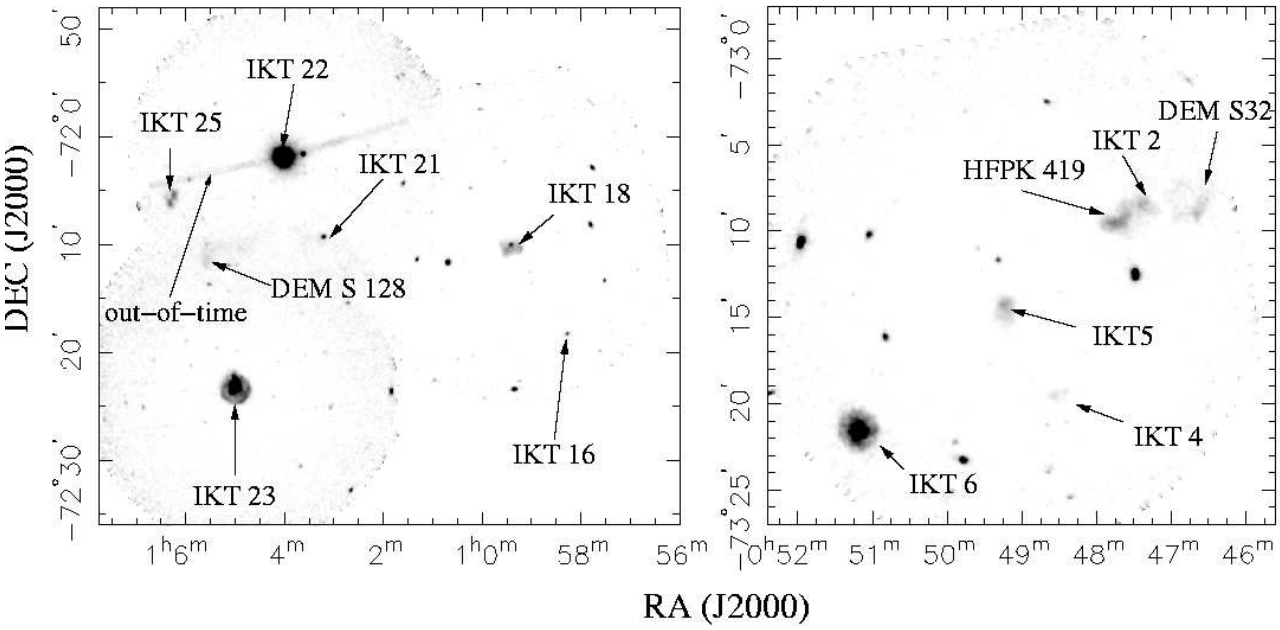

Fig. 1. Mosaic images of the SMC region. The left image is the combined observations of *XMM-Newton* Rev's 157, 247 and 433, while the right panel is an image of Rev 156. Individual remnants are indicated. The out-of-time events from IKT 22 can be seen .

We also estimated the electron density and radiating mass based on the best-fit emission measure. Here it is provisionally assumed that the emitting gas is confined to shells of a typical thickness R/12. The radii were estimated from the X-ray images. The mass estimates indicate that most of the sources are evolved remnants that have swept-up a considerable amount of mass and should thus be emitting in their Sedov phases. Moreover, a number of remnants could not be adequately described by the simple NEI model, in particular, the spectra with higher statistics (viz, IKT 6, IKT 22, IKT 23). These spectra appear to show an ionisation and/or temperature distribution. We thus consider a Sedov model to be the most appropriate for fitting the data. This model is based on the Sedov solution (Sedov 1959) which describes the self-similar expansion of an adiabatic blast wave in a homogeneous medium.

We proceed to fit the IKT 6, IKT 18, IKT 22 and IKT 23 spectra with a Sedov model, based on unacceptable χ^2's and large swept-up mass, obtained from the NEI model fits. IKT 6 and IKT 23 have a shell and centrally filled morphology. We extract and fit only the shell part of the spectra of these two remnants with a Sedov model. Even though IKT 22 is clearly less evolved than IKT 6 and IKT 23 (for example), we do find that the Sedov model provides a much better fit to the data. Hayashi et al. 1997 also found that Sedov model fits to the *A*SCA data of IKT 22 gave the most reliable results. We also fit, based on the high mass estimates for the NEI fits, the DEM S 32, IKT 2, HFPK 419, and IKT 16 spectra with a Sedov model.

The free parameters of the Sedov model are the normalisation ($n_{\rm e}n_{\rm H}R^3/d^2$), shock temperature ($T_{\rm s}$), ionisation parameter ($n_{\rm e}t_{\rm i}$), elemental abundances and the column density $N_{\rm H}$ of absorbing gas. Here $n_{\rm e}$ is the pre-shock electron density, $t_{\rm i}$ is the ionisation age of the remnant, R is the SNR shock radius and d is the distance to the source. The fitting procedure for the Sedov models is the same as in the case of the NEI models. The fit results are summarised in Table 4.

From these fits, we can estimate several physical parameters for the SNRs in question. If $n_{\rm e}$ is the electron density, $n_{\rm H}$ is the hydrogen density, $n_{\rm m}$ is the total number density of protons+neutrons (including those bound up in nuclei), then, using the elemental abundances and assuming a fully ionised plasma we can calculate the number of electrons per hydrogen atom $r_{\rm e} = n_{\rm e}/n_{\rm H}$ and the effective number of protons and neutrons (baryon mass) per hydrogen atom $r_{\rm m} = n_{\rm m}/n_{\rm H}$. By adopting the values of the parameters mentioned above we estimate the electron density ($n_{\rm e}$), the hydrogen density ($n_{\rm H}$), the Sedov dynamical age ($t_{\rm dyn}$), the effective ionisation age ($t_{\rm i}$), the total emitting mass (M) and initial explosion energy (E_0) by using:

$$n_{\rm e} = \sqrt{N r_{\rm e} d^2/R^3},\ {\rm m}^{-3} \quad (1)$$

$$n_{\rm H} = \sqrt{N d^2/(R^3 r_{\rm e})},\ {\rm m}^{-3} \quad (2)$$

$$t_{dyn} = 1.3{\times}10^{-14} R/\sqrt{T},\ {\rm yr} \quad (3)$$

$$t_i = 3.17{\times}10^{-8} I_{\rm t}/n_{\rm e},\ {\rm yr} \quad (4)$$

$$M = 5{\times}10^{-31} m_{\rm p} r_{\rm m} n_{\rm H} V,\ {\rm M}_\odot \quad (5)$$

$$E_0 = 2.64{\times}10^{-15} T R^3 n_{\rm H},\ {\rm J} \quad (6)$$

Here $m_{\rm p}$ is the proton mass, R is the shock radius, $V(= 4/3\pi R^3)$ is the total volume. We do not apply a volume filling factor to our estimates (eqs. 1–6) as it is already implicitely contained within the Sedov model. We assume that the remnants are spherically symmetric and therefore also do not apply a geometrical filling factor term to the volume estimate. The results are given in Table 5. The mass estimates based on the NEI fits compare well to those obtained from the Sedov model fits.

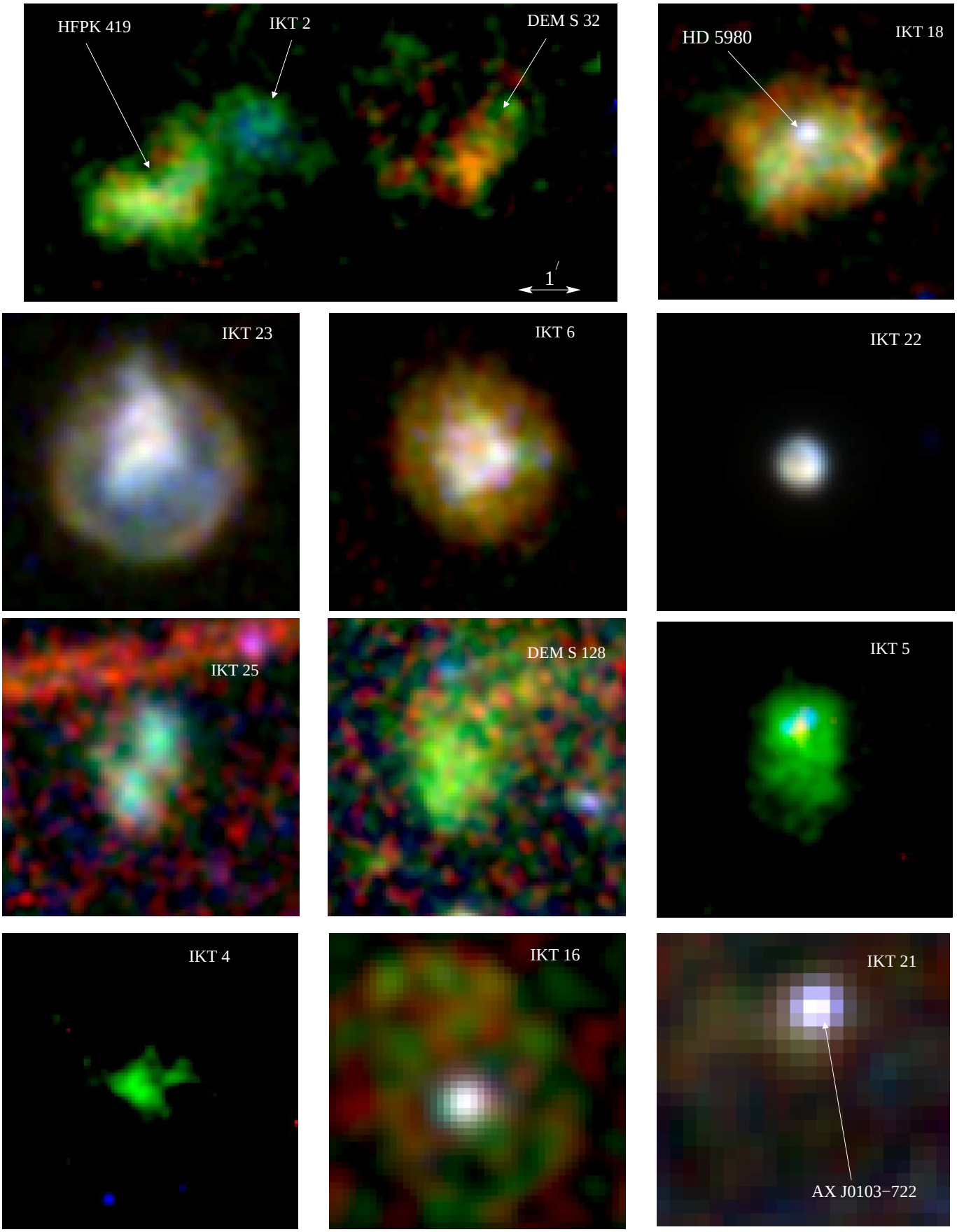

Fig. 2. Details of the remnants in our sample. Red, green and blue represents the 0.5–0.7 keV,0.7–1.0 and 1.0–3.0 keV energy bands. All the images are on the same plate scale.

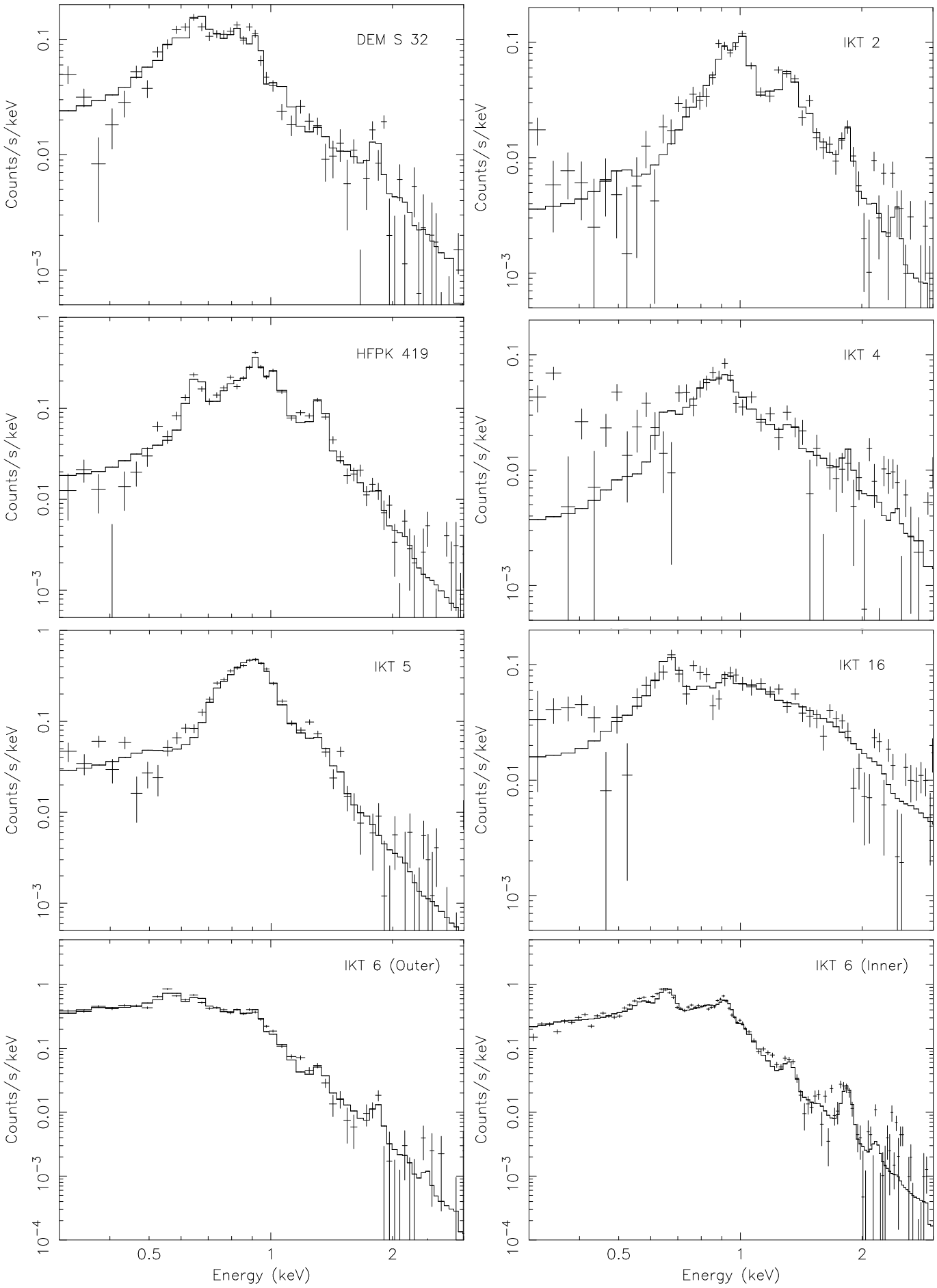

Fig. 3. Combined EPIC (i.e. EPIC-pn+EPIC-MOS) background-subtracted spectra of individual SNRs. The crosses represent the data points and error bars and the solid histogram represent the best fit models.

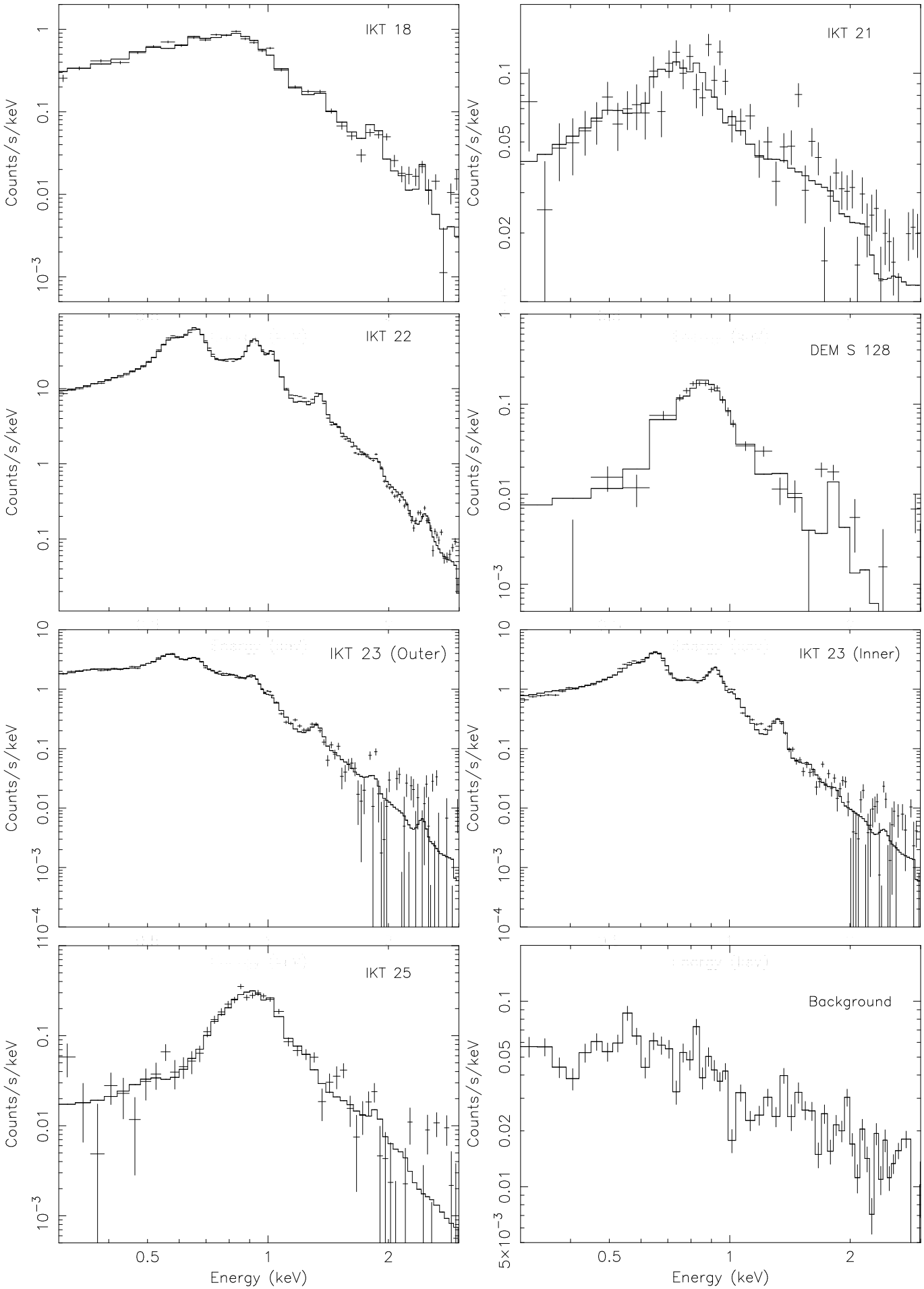

Fig. 4. Same as for Fig. 3. The lower right panel represents a typical background spectrum.

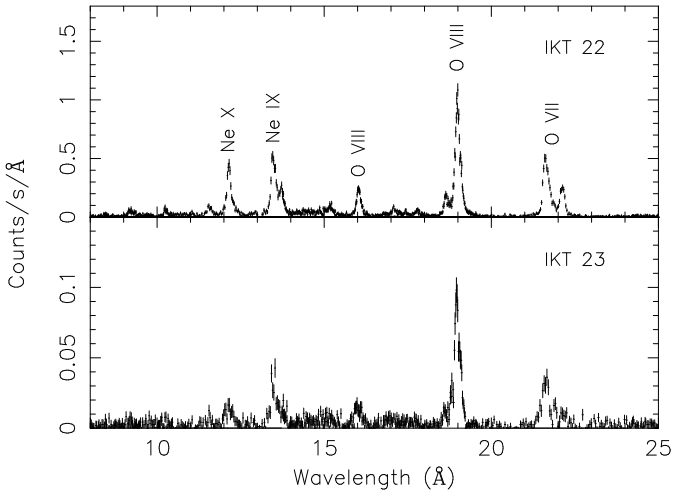

Fig. 5. RGS spectrum of IKT 22 (top) and IKT 23 (bottom). The most prominent emission lines are labeled.

Table 5. Physical parameters derived from the best fit Sedov model results.

SNR	n_e (10^6 m^{-3})	n_H	t_i (10^3 yrs)	t_{dyn} (10^3 yrs)	Mass ($M_\odot$)	E_0 (10^{44} J)
DEM S 32	0.05	0.05	15	6	43	0.9
IKT 2	0.45	0.44	>70	5.4	47	0.3
HFPK 419	0.26	0.25	>100	8.5	64	0.6
IKT 6	0.21	0.17	18	14	180	0.8
IKT 16	0.05	0.04	3.5	7.5	124	3.4
IKT 18	0.13	0.11	23	11	196	1.2
IKT 22	2.03	1.68	1.4	2.7	84	0.8
IKT 23	0.19	0.16	30	19	424	1.8

We also fit the spectra from the inner regions of IKT 6 and 23. As a model we use one NEI component to account for emission from the central region. In addition to this, we added the same plasma component and parameters as derived from the fits to the outer region, only the normalisations from these components were allowed to vary. This method accounts for any projected fore/background shell emission. The fit results supplied in Table 3, are very similar between the two remnants.

The best fit models generally provides good fits to the data, though a few discrepancies exist. Uncertainties in the modeling of the data include the calibration differences between the EPIC-pn and EPIC-MOS and incompleteness of the atomic database. For example, the most prominent residual is the underestimation of the spectra at $\approx$ 1.2 keV. This is a known problem and is probably due to missing high excitation lines of Fe XVII-XIX in the plasma code (see Brickhouse et al.2000).

4. Discussion

4.1. Progenitor Types

4.1.1. Core–Collapse candidates

IKT 2 and HFPK419 are located in the large emission nebuale N19. These remnants have rather irregular and complicated X-ray morphologies. For example, it is not clear whether IKT 2 and HFPK 419 are indeed two seperate remnants or part of a larger SNR. However, the spectra and derived abundances from these remnants are rather different. HFPK 419 shows enhanced O emission, while IKT 2 has virtually no discernible O emission. Also, IKT 2 has more enhanced Si emission. These differences presumably indicate that they indeed are separate objects. IKT 2 and HFPK 419 both show high metal abundances, which indicate that much of the X-ray emission is from ejecta enriched material. Their abundance profiles show a similar pattern in that the alpha-rich products O(except for IKT 2), Ne and Mg are higher than Fe. Enhanced O, Ne and Mg abundances usually indicates a core-collapse origin (e.g. Nomoto et al. 1997; Woosley & Weaver 1995). We thus suggest that these remnants are the results of core-collapse SNe. This is also in agreement with their surroundings which suggest at least modest starburst activity (Dickel et al. 2001).

DEM S 32 is also in the vicinity of N19. It has a shell-like structure with enhanced emission towards the southwestern limb. The abundance yields from DEM S 32 are lower than for IKT 2 and HFPK 419 and no clear distinction in progenitor type can be infered from these yields. The starburst vincinity, however, suggest that DEM S 32 possibly also originates from a core-collapse progenitor.

IKT 6 and IKT 23 are remarkably similar remnants, both morphologically and spectrally (Figs. 3 and 4). IKT 23 has a clear shell and a centrally filled morphology. The colours in Fig. 2 indicate that the outer region is softer than the inner region. IKT 6 exhibits a similar morphology, although it is not as clearly resolved. IKT 6 is located towards the edge of the detector where the effective area and spatial resolution is lower. The other remnant in our sample with a clear shell structure is IKT 22. This remnant is quite striking since it is orders of magnitude more luminous than the other SNRs in the field.

The spectra extracted from the two regions (i.e. outer and inner) of IKT 6 and IKT 23 (see Figs. 3 and 4) are distinctly different. However, the spectra are remarkably similar between the two remnants. The spectral fitting results given in Tables 3 and 4 also yield similar parameters for the two remnants. Although not clearly visible in the *XMM-Newton* data (because of the lower spatial resolution), the *Chandra* data do reveal that IKT 22 has a blastwave and reverse shock structure (Hughes et al. 2000). The spectra from these two regions are also distinctly different.

The abundance derived from the fits to the outer regions are consistent with the SMC ISM abundances, while the inner regions reveal much higher abundance values. We propose, based on the abundance profiles, that the inner region represents reverse shock heated ejecta material while the outer region represents a blastwave moving through the ISM/CSM. The fit results also show that the inner (ejecta-rich) regions are hotter ($kT \sim 0.9$ keV) than the outer regions ($kT \sim 0.27$ keV). This is expected from models such as proposed by Truelove and McKee 2001, which predict that the blastwave in more evolved remnants eventually attains a lower velocity than the reverse shock.

The spectra extracted from the inner regions of IKT 6 and IKT 23 are also similar to the IKT 22 spectrum. All three remnants show enhanced O, Ne and Mg abundances with respect

Table 3. NEI model spectral fitting results. The fit errors (1σ) are given in brackets. The abundances are all relative to their solar values (Anders & Grevese 1989).

SNR	Radius (arcsec)	$N_{\rm H}$ (10^{25} m^{-2})	$n_{\rm e}n_{\rm H}V$ (10^{64} m^3)	$kT_{\rm e}$ (keV)	$n_{\rm e}t$ (10^{16} m^{-3}s)	$n_{\rm e}$ (10^6) m^{-3}	Mass M$_\odot$
DEM S 32	68	2.4(0.7)	0.60(0.25)	1.51(0.48)	1.0(4.5)	0.18	39
IKT 2	33	3.9(1.5)	1.47(1.38)	0.77(0.59)	>20.0	0.84	21
HFPK 419	45	3.9(1.5)	1.21(1.1)	0.62(0.39)	>13.0	0.48	30
IKT 4	42	6.2(0.9)	0.14(0.03)	3.5(1.4)	2.1(0.2)	0.18	9
IKT 5	58	1.1(0.9)	0.47(0.23)	0.71(0.04)	>48.0	0.20	27
IKT 6	74	0.6(0.2)	5.89(0.8)	0.54(0.03)	3.5(0.4)	0.50	139
IKT 16	100	0.6(0.5)	1.91(0.42)	1.6(0.4)	0.37(0.07)	0.17	104
IKT 18	79	2.5(0.5)	9.13(3.5)	0.57(0.12)	2.7(+100)	0.56	190
IKT 21*	31	2.0(0.8)	0.48(0.31)	0.58(0.40)	4.3(+100)	0.53	11
IKT 22	24	1.1(0.1)	73.2(5.6)	0.38(0.01)	>600	9.62	93
IKT 23	99	0.41(0.12)	9.3(1.3)	0.68(0.04)	2.5(0.4)	0.41	270
DEM S 128	62	1.8(1.2)	0.17(0.1)	0.61(0.1)	>200	0.11	18
IKT 25	55	4.8(1.7)	1.20(0.5)	0.60(0.1)	38(20.0)	0.36	40
IKT6-inner	30	0.8(0.1)	0.13(0.06)	0.89(0.16)	5.4(2.1)	0.29	5
IKT23-inner	40	1.1(0.1)	0.22(0.08)	0.92(0.12)	2.8(0.5)	0.25	11

SNR	O	Ne	Mg	Si	Fe	L_x(0.5-2 keV) (10^{27} W)	χ^2/d.o.f
DEM S 32	0.20(0.06)	0.23(0.08)	<0.10)	0.29(0.21)	0.08(0.05)	19	190/151
IKT 2	<0.10	0.81(0.42)	0.72(0.35)	0.41(0.13)	0.13(0.09)	14	152/155
HFPK 419	1.21(0.9)	1.91(1.5)	1.64(1.4)	0.24(0.2)	0.39(0.34)	42	192/155
IKT 4	0.2(f)	0.2(f)	0.2(f)	0.2(f)	0.2(f)	18	205/155
IKT 5	<0.1	0.92(0.65)	0.93(0.45)	<0.1	0.91(0.35)	9.6	340/320
IKT 6	0.11(0.01)	0.24(0.03)	0.17(0.04)	0.42(0.2)	0.09(0.01)	66	610/320
IKT 16	0.20(f)	0.20(f)	0.20(f)	0.20(f)	0.20(f)	61	162/109
IKT 18	0.06(0.02)	0.09(0.04)	0.07(0.03)	0.25(0.1)	0.07(0.1)	62	333/153
IKT 21	0.20(f)	0.20(f)	0.20(f)	0.20(f)	0.20(f)	8.0	416/361
IKT 22	2.03(0.14)	2.46(0.24)	1.50(0.06)	0.65(0.09)	0.10(0.01)	150	3043/212
IKT 23	0.14()	0.28()	0.21()	0.00()	0.07()	150	1103/320
DEM S 128	0.00()	0.00()	2.60(1.8)	2.43(1.6)	2.34(1.1)	7.8	125/115
IKT 25	<0.1	3.01(1.2)	<0.1	<0.1	1.53(0.4)	45	139/156
IKT6-inner	2.0(0.6)	2.3(0.8)	1.6(0.9)	2.7(1.2)	0.87(0.31)	17	180/155
IKT23-inner	2.1(0.5)	4.7(1.2)	3.3(1.3)	0.2(f)	0.55(0.15)	37	410/320

* plus power-law component, norm.$\sim 2.2\times10^{43}$ phs^{-1}keV^{-1} and $\gamma \sim 0.9$
$^+$f - fixed

to Fe. The abundance values of these elements (w.r.t. solar) are also an order of magnitude larger than their SMC ISM values. We also obtained RGS spectra of IKT 22 and IKT 23. The spectra were extracted from the entire remnants. The high-resolution RGS spectra of IKT 22 and IKT 23, displayed in Fig. 5, again bear striking similarities and reveal prominent emission lines of O and Ne species. The most obvious difference between the two spectra is in the count rate. The flux in the emission lines of IKT 22 are an order of magnitude larger than compared to IKT 23. Much of this flux difference can be attributed to the differences in abundance values. This is because the RGS (and EPIC) spectrum of IKT 22 is dominated by emission from ejecta-rich material, while the IKT 23 spectrum is dominated by emission from the swept-up ISM material, which has an average abundance of ~ 0.2 solar. Fits to the EPIC data extracted from the entire remnant also show that the abundances for IKT 22 are an order of magnitude larger than compared to IKT 23. A more detailed RGS analysis of IKT 22 is provided by Rasmussen et al. (2001).

The similarities between IKT 6, IKT 22 and IKT 23 suggests that these three remnants have common progenitors. IKT 22 is a well studied remnant that has been classified as being the result of a type II SN. IKT 6 and IKT 23 should thus also be the remnants of type II SNe. Both the derived abundances and masses for the inner regions of IKT 6 and IKT 23 are consistent with this interpretation. These remnants represent very different stages of SNR evolution. IKT 22 is a $\sim$2 000 yr old remnant (Blair et al. 1989) while IKT 6 an IKT 23 are much more evolved (14 000–20 000 yr). We propose that IKT 6 and IKT 23 are evolved versions of IKT 22 and studying these remnants in more detail presents a unique opportunity to probe the evolution of oxygen-rich remnants in the SMC. It is also interesting to note that the ejecta are still visible in remnants as evolved as IKT 6 and IKT 23.

IKT 16 is one of the weaker X-ray sources in our sample. The X-ray morphology appears consistent with the radio and Hα classification of it being a shell like SNR (Mathewson et al. 1984). A harder emission spot can be seen in the centre of the X-ray image. We attempted to extract a separate spectrum

Table 4. Sedov model spectral fitting results. The fit errors (1σ) are given in brackets. The abundances are all relative to their solar values (Anders & Grevese 1989).

SNR	$N_{\rm H}$ (10^{25} m^{-2})	$n_{\rm e}n_{\rm H}R^3/d^2$ (10^{20} m^3)	$kT_{\rm e}$ (keV)	$n_{\rm e}t$ (10^{16} m^{-3}s)	$\rm L_x(0.5-2keV)$ (10^{27} W)	
DEM S 32	1.9(0.6)	1.70(0.7)	1.29(0.46)	2.5(1.1)	16	
IKT 2	5.1(1.2)	16.3(9.3)	0.39(0.05)	>220	20	
HFPK 419	4.4(0.9)	12.7(5.2)	0.28(0.03)	>360	57	
IKT 6	0.7(0.25)	22.5(7.5)	0.27(0.05)	11.1(0.5)	39	
IKT 16	5.1(0.6)	4.32(1.8)	1.76(0.65)	0.51(0.1)	39	
IKT 18	1.3(0.25)	15.4(5.1)	0.51(0.06)	20.0(10.1)	39	
IKT 22	0.60(0.06)	99.3(11)	0.78(0.08)	9.0(+1.7)	1.3×10^3	
IKT 23	0.5(0.1)	51.9(5.8)	0.26(0.03)	20.0(0.4)	85	
SNR	O	Ne	Mg	Si	Fe	χ^2/d.o.f
DEM S 32	0.28(0.15)	0.17(0.14)	0.19(0.14)	0.45(0.26)	0.23(0.1)	164/149
IKT 2	<0.08	0.89(0.39)	0.51(0.23)	0.33(0.17)	<0.1	152/149
HFPK 419	1.25(0.45)	2.19(0.74)	1.65(0.54)	0.13(0.1)	0.25(0.1)	193/150
IKT6-outer	0.13(0.03)	0.28(0.08)	0.3(0.12)	0.4(0.3)	0.15(0.04)	223/155
IKT 16	0.2(f)	0.2(f)	0.2(f)	0.2(f)	0.2(f)	199/165
IKT 18	0.14(0.07)	0.11(0.07)	0.22(0.09)	0.44(0.13)	0.17(0.03)	253/153
IKT 22	0.87(0.05)	1.99(0.10)	1.32(0.09)	0.21(0.03)	0.29(0.02)	841/211
IKT23-outer	0.17(0.02)	0.28(0.04)	0.35(0.07)	0.36(0.15)	0.11(0.02)	460/320

from this region, but the data is of insufficient quality to speculate on the X-ray nature of this region. A longer exposure observation is needed to investigate whether this source is thermal or non-thermal in nature.

Also interesting is the high explosion energy ($\sim3.3\times10^{44}$ W) and low ionisation age ($t_{\rm i}\sim3\,500$ yr) associated with IKT 16. The fit parameters are not very well constrained due to the low count rate so the discrepancies might originate from statistical limitations. However, in their analysis of the LMC remnants, Hughes et al. 1998 found a connection between low ionisation age (as compared to the dynamical age) and high explosion energy. They explain this connection as SNRs which exploded within pre-existing low-density cavities in the ISM. The remnant expands rapidly to the cavity wall, where it then encounters denser gas and begins to emit X-rays. This results in a lower dynamical age and explosion energy than that inferred from the Sedov model. A similar scenario could thus be applicable to IKT 16. If this is the case, then IKT 16 would be the result of the core-collapse of a massive star whose stellar wind has caused a low density circumstellar cavity.

There is no clear X-ray emission associated with the optical emission from IKT 21, however, our X-ray image (Fig. 2) does show some faint, diffuse emission extending to the east of the Be-pulsar binary system AX J0103-722 (Israel et al. 2000). The X-ray emission from the vicinity of the optical remnant is, however, dominated by the puslar system.

We extracted our spectrum from the region containing the optical emission, which includes the pulsar system. Although not visible in Fig. 4, the spectrum clearly extends above 3 keV. Our model for IKT 21 thus consists of a NEI component for thermal emission from the SNR and a power-law component to account for the pulsar emission. The power-law component normalisation and photon index were initialy fixed to values obtained from Hughes and Smith 1998 and were subsequently allowed to vary. The best fit model gives a power-law component normalisation of $\sim\ 2.2\times10^{43}$ phs^{-1}keV^{-1}, a photon index of $\sim\ 0.9$ and a luminosity of $\sim\ 5.5\times10^{27}$ W(0.5–2.0 keV band). Our results for the thermal emission indicate a temperature of $kT_{\rm e}\sim0.58\pm0.40$ and a luminosity of $\sim\ 8\times10^{27}$ W (0.5–2.0 keV band). These results compare well with estimates obtained by Hughes and Smith 1998. It is not clear whether the pulsar AX J0103-722 is associated with the SNR as it is not near the centre of the remnant. An association would mean that IKT 21 would be the remnant of a massive-star SN (Hughes and Smith 1998).

4.1.2. Type Ia candidates

The images in Fig. 2 show that IKT 4, IKT 5, DEM S 128 and IKT 25 have similar diffuse X-ray morphologies with no clear shell like structure. The emission peaks in the 0.7–1.0 keV band. This indicates that the flux of these sources are dominated by emission from Fe-L transitions. These four remnants also have similar spectral features. They show a broad spectral hump around the Fe-L complex ($\sim\ 0.9$ keV). The excess emission around $\sim\ 0.9$ keV and the high Fe abundance in these remnants strongly suggests that these remnants are the result of type Ia supernovae.

The X-ray sizes of IKT 4, IKT 5, DEM S 128 and IKT 25 are much smaller than their optical diameters (see Mathewson et al. 1983 and Mathewson etal. 1984). The large optical diameters imply that they are evolved remnants. Mathewson et al. (1984) also attributes the high S II emission detected in IKT 5 and IKT 25 to the onset of radiative cooling due to the evolved nature of these remnants. A possible interpretation is that these remnants are much more evolved versions of SNR DEM L 71 in the LMC (Hughes et al. 2003;van der Heyden et al. 2003). Here we see a bright ISM dominated shell with fainter Fe-rich ejecta material in the centre. In this scenario, IKT 4, IKT 5, DEM S 128 and IKT 25 would have evolved to such a degree

that the shells have eventually become too faint or too cool to be seen in X-rays and we only see the hotter Fe-rich ejecta remains. The morphologies and temperature structure of IKT 6 and IKT 23 also add credence to such a scenario.

The mass estimates given in Table 3 was made on the assumption that the X-ray emission is from shock heated ISM material. However, if the emission is from the ejecta remains then the metals (and not H) would be the main source of the X-ray emission. This will alter our mass estimates. The mass, however, depends on the amount of H mixed into the ejecta during its evolution (see Hughes et al. 2003 for a complete explanation). If we assume that a comparable amount (in mass) of hydrogen has been mixed into the metal rich ejecta then this would give Fe mass estimates of 0.4, 0.8, and 0.67 $M_{\odot}$ for IKT 5, IKT25 and DEM S 128 respectively. These estimates are within the Fe mass range given by Nomoto et al. (1997) for various type Ia SNe models. We do not make mass estimates for IKT 4 since the quality of the data does not allow for accurate abundance determination.

4.1.3. The special case of IKT 18

IKT 18 has a rectangular shape. The emission is diffuse with no obvious limb brightening. The *Chandra* data (Nazé et al. 2002) do reveal a few bright or dark arcs, but apart from these, the brightness is rather uniform. The luminous blue variable (LBV) HD 5980 can also be seen in the centre of IKT 18. The spatial coincidence of IKT 18 with the peculiar binary system HD 5980 suggests an association with this system. The possible association was recently investigated by Nazé et al. (2002). They drew attention to similarities between IKT 18 and the Carina nebula. However, they concluded that based on the non-thermal radio emission (Ye et al. 1991) and a high velocity expansion (Chu & Kennicutt 1988), IKT 18 should be regarded as a SNR with HD 5980 located behind the remnant. The low SMC-like abundances and high mass (196 $M_{\odot}$) and age estimate (11 000 yr) derived from our fits are also consistent with the picture of an evolved SNR which has swept-up ISM material. The low abundances, however, do not allow for a progenitor typing. More *XMM-Newton* data will be available in the near future, which will allow for a more detailed assessment of the nature of this object.

4.2. SMC Abundances

The abundance values for the swept-up matter dominated SNRs (Table 4) show some spread among the remnants and also between different elemental species. The general trend is that the larger remnants have lower abundance values while the smaller ones have larger values. The interpretation is that the older remnants have swept-up so much ISM material that the abundances are approaching the ISM values. The abundance yields from the older remnants with larger swept-up masses could thus be used to probe the ISM abundance distribution.

We use the abundances derived from the spectral fits to IKT 6 (outer region), IKT 18 and IKT 23 (outer region) to determine the gas-phase abundances of the SMC. These remnants are selected because of their high (swept-up) masses. We average, for each elemental species, the fitted abudances from the three remnants. In Fig. 6 we plot the error weighted average abundances versus elemental species. The uncertainties represent the rms-scatter among the remnants. The derived abundances are also compared to the average SMC abundance values presented by Russel & Dopita (1992). The work of Russel & Dopita (1992) is based on the spectral analysis of F supergiants for heavier elements (Z$>$ 12) and H II regions and SNRs for lower Z elements. However, they only have 1 SMC SNR in their studies. Our average abundance values for the low-Z elements appear slightly higher than those obtained by Russel & Dopita (1992), but are in good agreement within the uncertainties.

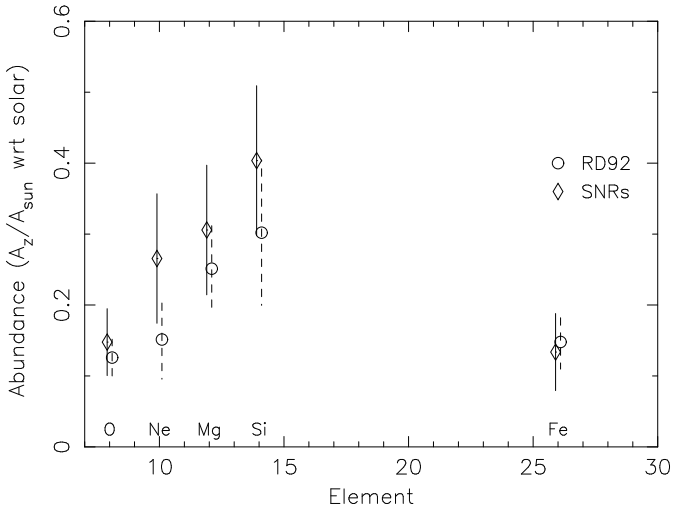

Fig. 6. Average SMC abundances. The average abundance values obtained from fits to IKT 6 IKT 18 and IKT 23 are represented by diamonds. Results from Russel & Dopita (1992) are indicated with circles.

4.3. Physical parameters

The ionisation ages given in Table 5 are generally consistent with the dynamical age within a factor 2, the exceptions being IKT 2 and HFPK 149. The factor of 2 difference can be easily explained invoking fragmentary shells or clumping of the X-ray emitting gas. This would increase the electron density and thus reduce the ionisation age estimates. The possibility of fragmentary shells or clumping means that the initial explosion energy E_0 and mass estimates should be regarded as lower and upper bounds respectively.

In the case of IKT 2 and HFPK 149 the plasma has reached ionisation equilibrium. In this regime the ionisation parameter becomes insensitive as an age indicator since the spectrum changes very slowly with increasing ionisation parameter.

The mean SMC ISM hydrogen density derived from the Sedov model fits is $\sim 0.32\times10^{6}$ m^{-3}. This is nearly an order of magnitude lower than the mean density of $\sim 1.8\times10^{6}$ m^{-3} derived from Sedov fits to a sample of LMC remnants by Hughes et al. 1998. The lower SMC abundance easily explains the lower SNR luminosities compared to their LMC counter-

parts, as the X-ray emission scales with the square of the densities. The lower densities also have implications for the dynamical evolution of SNRs in the SMC. Falle et al. (1981) predicts that the onset of radiative cooling occurs at a time $t_{\rm cool} = 3.55{\times}10^7 E_{44}^{0.24} n_H^{-0.52}$ yr, where E_{44} is the explosion energy in 10^{44} W and n_H is in m^{-3}. The onset of radiative cooling will be governed by the hydrogen density, since the explosion energies derived from the SMS and LMC samples are similar. The lower hydrogen density means that the SMC remnants takes ~ 2.5 times longer to reach the radiative cooling stage, compared to the LMC remnants. The SMC remnants should thus be radiating X-rays for a longer time than in the LMC. This point is illustrated by the fact that oldest remnant in our sample is ∼20 000 yr while the oldest remnant in the LMC sample analysed by Hughes et al. 1998 is 10 000 yr.

4.4. SN rates

We identified 8 core-collapse (II+Ib/c) and 4 type Ia remnants in Sect. 4.1 and make simple SNe rate estimates, since the statistics do not allow for more involved calculations. By dividing the number of SNRs by the age of the oldest remnant we get a core-collapse SNe rate of one per 2 400±800 yr. The error accounts for the statistical uncertainty and incompleteness of our sample. This is much lower than an estimate by Filipovic et al. (1998) who give a birth-rate of one SNR per 350 yr. Their result is based on a relation between the SNR age and radio flux. Our result is more in line with a rate of one in every 1100–2500 inferred from van den Berg & Tammann (1991), which is derived from the star formation rate inferred from the total Hα luminosity of the SMC. The derived rate is also consistent with our age estimate ($\sim 2\,700$ yr) of the youngest SMC SNR (viz. IKT 22). The number of type Ia SNRs is approximately 0.5 that of core-collapse, which implies a frequency of one in every 4 800±1 600 yr.

Acknowledgements. We thank Jacco Vink for the use of and help with his image processing software and for valuable discussions. The results presented are based on observations obtained with XMM-Newton, an ESA science mission with instruments and contributions directly funded by ESA Member States and the USA (NASA). SRON is supported financially by NWO, the Netherlands Organisation for Scientific Research.

References

Anders, E., & Grevese, N., 1989, Geochimica et Cosmochimica Acta, 53, 197
van den Berg, S., & Tammann, G., 1991, ARA&A, 29, 363
Blair, W.P., Raymond, J.C., Danziger, J., Matteucci, F., 1989, ApJ, 338, 812
Brickhouse, N. S., Dupree, A. K., Edgar, R. J., et al., 2000, ApJ, 530, 387
Cappellaro, E., Evans, R., & Turrato, M., 1999, A&A, 351, 459
Chu, Y.-H, & Kennicutt, R.C., 1988, AJ, 95, 1111
Davies, R.D., Elliot, K.H., & Meaburn, J., 1976, Royal Astronomical Society, Memoirs, 81, 89.
Dickel, J.R., Williams, R.M., Carter, L.M., Milne, D.K., Petre, R., Amy, S.W. 2001, AJ, 122, 849
Falle, S.A.E.G., 1981, MNRAS, 195, 1011
Filipovic, M.D., Pietsch, W., Haynes, R.F., et al., 1998, A&ASS, 127, 119
Haberl, F., Filipovic, M.D., Pietsch, W., & Kahabka, P., 2000, A&ASS, 142, 41
Hayashi, I., 1997, PhD thesis, Graduate School of Science, Kyoto University
den Herder, J.W., Brinkman, A.C., Kahn, S.M., et al., 2001, A&A, 365, L7
van der Heyden, K.J., Bleeker, J.A.M, Kaastra, J., & Vink, J., 2003, A&A, 406, 141
Hughes, J.P., Smith, R.C., 1994, AJ, 107, 1363
Hughes, J.P., Hayashi, I., & Koyama, K., 1998, ApJ, 505, 732
Hughes, J.P., Rakowski, C.E., & Decourchelle, A., 2000, ApJ, 543, L61
Hughes, J.P., Ghavamian P., Rakowski C.E., & Slane, P., 2003, ApJ, 582, L95
Inoue, H., Koyama, K., & Tanaka, Y., 1983, in IAU Symposium 101, Supernova Remnants and Their X-ray Emission, ed. P. Gorenstein & J. Danziger (Dordrecht; Reidel), p535
Israel, G.L., Campana, S., Covino, S., et al.,2000, ApJ, 531, L131
Kaastra, J.S., Mewe, R., & Nieuwenhuijzen, H. 1996, in UV and X-ray Spectroscopy of Astrophysical and Laboratory Plasmas, p. 411, eds. K. Yamashita & T. Watanabe, Tokyo, Univ. Ac. Press
Massey, P., Lang, C.C., DeGioia-Eastwood, K., Garmany, C.D., 1995, ApJ, 438, 188
Mathewson, D.S., Ford, V.L., Dopita, M.A., Tuohy, I.R., Long, K.S., & Helfand, D.J., 1983, ApJS, 51, 345
Mathewson, D.S., Ford, V.L., Dopita, M.A., Tuohy, I.R., Mills, B.Y., & Turtle A.J., 1984, ApJS, 551, 189
Mewe, R., Kaastra, J.S., & Liedahl, D.A., 1995, Legacy 6, 16
Nazé, Y., Hartwell, J. M., Stevens, I. R., et al., 2002, ApJ, 580, 225
Nishiuchi, M., 2001, PhD Thesis, Kyoto University
Nomoto, K., Iwamoto, K., Nakasato N., et al., 1997, Nucl. Phys. A, 621, 467
Rasmussen, A., Behar, E., Kahn, et al., 2001, A&A, 365, L231
Russel, S.C., & Dopita, M.a., 1992, ApJ, 384, 509
Sedov, L.I., 1959, Similarity and Dimensionless Methods in Mechanics (New York:Academic)
Strüder, L., Briel, U.G., Dennerl, K., et al., 2001, 365, L18
Truelove, J. K., & McKee, C. F., 1999, ApJS, 120, 299
Turner, M.J.L., Abbey, A., Arnaud, M., et al., 2001, 365, L27
Wang, & Q., Wu, X., 1992, ApJS, 78, 391
Woosley, S.E., & Weaver, T.A., 1995, ApJS, 101, 181
Ye, T., Turtle, A.J., & Kennicutt, R.C., 1991, MNRAS, 249, 722